Spectral Retrieval of Latent Heating Profiles from TRMM PR Data. Part I: Development of a Model-Based Algorithm

SHOICHI SHIGE

Earth Observation Research and Application Center, Japan Aerospace Exploration Agency, Tokyo, Japan

YUKARI N. TAKAYABU

Center for Climate System Research, University of Tokyo, Tokyo, Japan

WEI-KUO TAO

Laboratory for Atmospheres, NASA Goddard Space Flight Center, Greenbelt, Maryland

DANIEL E. JOHNSON

Laboratory for Atmospheres, NASA Goddard Space Flight Center, Greenbelt, and Goddard Earth Sciences and Technology Center, University of Maryland, Baltimore County, Baltimore, Maryland

(Manuscript received 10 January 2003, in final form 4 February 2004)

ABSTRACT

An algorithm, the spectral latent heating (SLH) algorithm, has been developed to estimate latent heating profiles for the Tropical Rainfall Measuring Mission precipitation radar with a cloud-resolving model (CRM). Heating-profile lookup tables for the three rain types—convective, shallow stratiform, and anvil rain (deep stratiform with a melting level)—were produced with numerical simulations of tropical cloud systems in the Tropical Ocean and Global Atmosphere Coupled Ocean–Atmosphere Response Experiment. For convective and shallow stratiform regions, the lookup table refers to the precipitation-top height (PTH). For the anvil region, on the other hand, the lookup table refers to the precipitation rate at the melting level instead of PTH. A consistency check of the SLH algorithm was also done with the CRM-simulated outputs. The first advantage of this algorithm is that differences of heating profiles between the shallow convective stage and the deep convective stage can be retrieved. This is a result of the utilization of observed information, not only on precipitation type and intensity, but also on the precipitation depth. The second advantage is that heating profiles in the decaying stage with no surface rain can also be retrieved. This comes from utilization of the precipitation rate at the melting level for anvil regions.

1. Introduction

Tropical precipitating cloud systems are one of the most important elements of the global climate system. The latent heat released by precipitating cloud systems is the primary agent of the vertical energy transport from the surface to the atmosphere. The excess of radiative energy gained at the lower-latitude surface, thus, participates in the atmospheric general circulation (Simpson 1992).

A great many studies have examined the roles of tropical precipitation in maintaining atmospheric circulations on many scales, ranging from mesoscale to synoptic to planetary (e.g., Matsuno 1966; Gill 1980; Hartmann et al. 1984; Yoshizaki 1991; Mapes 1993; Shige and Satomura 2000). Although there have been disputes on the interactions between tropical large-scale atmospheric circulations and convection (Emanuel et al. 1994; Stevens et al. 1997; Mapes 1997), early studies in the Marshall Island areas (Nitta 1970, 1972) and recent Tropical Ocean and Global Atmosphere (TOGA) Coupled Ocean–Atmosphere Response Experiment (COARE)[1] studies over the warm-pool region have shown that convection plays an important role in the large-scale dynamics (see a review of Stevens et al. 1997). Yanai et al. (2000) have shown that during TOGA COARE the conversion of perturbation available

---

Corresponding author address: Dr. Shoichi Shige, Department of Aerospace Engineering, Osaka Prefecture University, 1-1 Gakuen-cho, Sakai, Osaka 599-8531, Japan.
E-mail: shige@aero.osakafu-u.ac.jp

[1] TOGA COARE was conducted over the western Pacific Ocean warm pool from November 1992 to February 1993.

potential energy generated by convective heating maintains the perturbation kinetic energy of the intraseasonal oscillations (ISO; Madden and Julian 1971, 1972, 1994), which occasionally influence large-scale climate shifts, such as El Niño (Takayabu et al. 1999).

Houze (1982) and Johnson and Young (1983) emphasized the differences of diabatic heating profiles that exist between convective and stratiform regions of mesoscale convective systems (MCSs). They found that for convective regions of MCSs the heating profile has warming at all levels with a maximum at midlevels, whereas in stratiform regions there is a warming peak in the upper troposphere and a cooling peak at low levels. The resulting MCS heating profile is positive at all levels, but with a maximum value in the upper troposphere. Hartmann et al. (1984) demonstrated that the heat source resembling a heating profile of MCSs with a maximum value in the upper troposphere produces a Walker circulation, which is in much better agreement with observations than those that are produced with a more conventional heat source (resembling a convective heating profile) with a simple linear global model.

The Tropical Rainfall Measuring Mission (TRMM), a joint Japanese–U.S. cooperative Earth probe satellite, was successfully launched in 1997 to advance understanding of the global energy and water cycle (Kummerow et al. 2000). The precipitation radar (PR) and the TRMM Microwave Imager (TMI) have been providing distributions of rainfall throughout the Tropics and have contributed significantly toward reducing uncertainty in satellite estimates of rainfall. The primary goal of TRMM is to use this precipitation information to determine the four-dimensional (i.e., temporal and spatial) patterns of latent heating over the whole tropical region.

Tao et al. (2001) used TRMM precipitation information to estimate the four-dimensional latent heating structure over the global Tropics for 1 month (February 1998). Three different latent heating algorithms—the hydrometor heating (HH; Yang and Smith 1999a,b), the convective–stratiform heating (CSH; Tao et al. 1993a), and the Goddard profiling (GPROF) heating (Olson et al. 1999) algorithms—were used and their results were intercompared. The HH and GPROF algorithms are microwave radiometer based for the TMI. Only for one of the three algorithms, the CSH algorithm, can PR products be used as input, as well as TMI products. This is because the CSH algorithm utilizes only the surface rain rate and an estimate of the fractions of rainfall produced by convective and stratiform processes. The CSH algorithm assumes that the shape of the overall MCS heating profile is determined by the relative amounts of convective and stratiform heating, which are proportional to the relative amounts of convective and stratiform precipitation.

The first spaceborne precipitation radar, PR provides height information based upon the time delay of the precipitation-backscattered return power and has enabled us to directly obtain vertical profiles of precipitation over the global Tropics (Kozu et al. 2001; Okamoto 2003). The classification between convective and stratiform rain became more straightforward utilizing observed precipitation profiles (Awaka et al. 1998). The accuracy of this classification is very important for estimating latent heating (Houze 1997). Moreover, the observed precipitation profiles should be related to those of latent heating (Tao et al. 1990). Thus, the accuracy of latent heating estimates from the PR should be superior to that from the TMI, which measures radiances that are the end product of the integrated effects of electromagnetic absorption/emission and scattering through a precipitating cloud along the sensor view path.

The concept of a spectral approach originates from Austin and Houze (1973) and Houze (1973) in which the precipitation-top height (PTH) observed by surface-based radar data was utilized in estimating the vertical transports by cumulus-scale convection. This spectral approach has been extended by Houze and Leary (1976), Leary and Houze (1980), Houze et al. (1980), and Cheng and Houze (1980). Takayabu (2002) used a similar concept and obtained a spectral expression of precipitation profiles to examine convective and stratiform rain characteristics statistically over the equatorial area (10°N–10°S) observed by the TRMM PR. In her study, all nadir data of PR2A25 version 5 (Iguchi et al. 2000) for the period of 1998–99 were utilized. Precipitation profiles with a 0.3 mm h^{-1} precipitation-top threshold were accumulated and stratified by PTHs. The threshold of 0.3 mm h^{-1} corresponds to 17.2 (stratiform) and 15.5 (convective) dBZ above the 0°C height and 17.0 (stratiform) and 14.2 (convective) dBZ just below the 0°C height in typical initial equivalent reflectivity factor–rainfall rate (Z_e–R) relations used in the PR2A25 version-5 algorithm (Iguchi et al. 2000). Properties of convective rain profiles show near-monotonic change with cumulative frequency. Stratiform rain profiles consist of two groups. One group consists of shallow stratiform rain profiles, which are very weak and increase downward. The other group consists of anvil rain profiles, characterized by maximum intensity around the melting level, much less intensity above, and a downward decrease below as indicated in traditional radar observations.

Based on the results of spectral precipitation statistics of Takayabu (2002), we introduce a new retrieval algorithm for latent heating estimates utilizing the TRMM PR data. It is named the spectral latent heating (SLH) algorithm and utilizes a cloud-resolving model (CRM) to produce its spectral lookup tables. The primary difference from the CSH algorithm is that the SLH algorithm requires information about not only convective/stratiform characteristics and surface precipitation rate, but also about the precipitation profile. The total heating profile shape is affected basically by two factors: the fraction of stratiform rainfall and the shape of the convective heating profile. The importance of the first factor

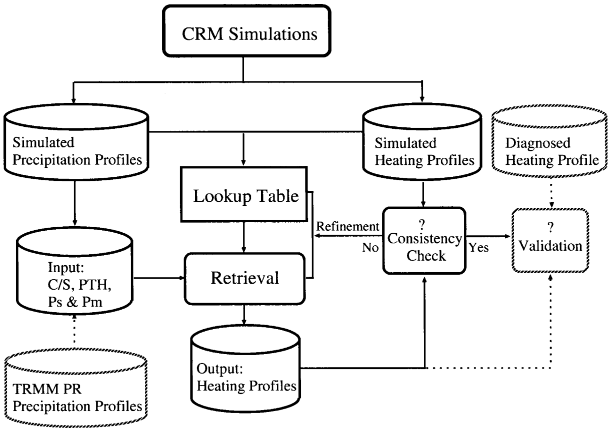

FIG. 1. Diagram showing the procedure for deriving and validating the SLH algorithm. Letters denote convective and stratiform classification (C/S), PTH, the precipitation rate at the observable lowest level (P_s), and the precipitation rate at the melting level (P_m). The "?" means to compare and examine the heating profiles reconstructed from the SLH algorithm with the heating profiles from model simulations. This consistency check is a necessary precondition for the application of the algorithm to actual TRMM PR data.

has been shown by Johnson (1984) and has been taken into account by the CSH algorithm. By utilizing the information about precipitation profiles, the second factor is also taken into account by the SLH algorithm.

This paper will describe the procedure of the SLH algorithm. A set of heating-profile lookup tables for convective, shallow stratiform, and deep stratiform (anvil) regions with melting levels are produced with numerical simulations of tropical cloud systems in TOGA COARE. A consistency check of the SLH algorithm will also be done with the CRM-simulated outputs in this paper.

2. Approach

Figure 1 shows the procedure for deriving the SLH algorithm. As well as for the CSH algorithm, a set of lookup tables is produced from CRM-simulated heating profiles. The primary difference from the CSH algorithm's lookup table is that the SLH algorithm's lookup table refers to the PTH of corresponding CRM-simulated precipitation profiles. Because of the scarcity of reliable validation data and difficulties associated with the collocation of validation data and satellite measurements, a consistency check of the SLH algorithm is performed using CRM-simulated precipitation profiles as a proxy for the PR data. The algorithm-reconstructed heating profiles from CRM-simulated precipitation profiles are compared with CRM-simulated "true" heating profiles, which are computed directly from the model thermodynamic equation. The consistency check is a useful and necessary precondition for the application of the algorithm to actual TRMM PR data.

a. CRM simulations

The CRM used in this study is the two-dimensional version of the Goddard Cumulus Ensemble (GCE) model, and is primarily documented in Tao and Simpson (1993). Recent improvements were presented in Tao (2003) and Tao et al. (2003). The GCE model has been used to develop the other TRMM heating algorithms, namely, the CSH and GPROF algorithms.

Here, we introduce a brief summary of the model configuration. The model includes solar and infrared radiative transfer processes and explicit cloud–radiation interactive processes (Tao et al. 1996). Simulations presented in this study employ a parameterized Kessler-type two-category liquid water scheme (cloud water and rain) and a three-category ice-phase scheme (cloud ice, snow, and graupel) by Rutledge and Hobbs (1984). Subgrid-scale (turbulent) processes in the GCE model are parameterized using a scheme based on Klemp and Wilhelmson (1978) and Soong and Ogura (1980). The effects of both dry and moist processes on the generation of subgrid-scale kinetic energy have been incorporated in the model. The model domain is 1024 km in the x direction (horizontal) and 22.4 km in the z direction (vertical). The horizontal resolution is 1000 m. The vertical resolution varies from 100 m at the lower boundary to 1000 m at the top of the domain.

In this study, tropical convective systems in TOGA COARE are simulated with the so-called *cloud ensemble modeling* approach. In this approach, many clouds of different sizes in various stages of their life cycles can be present at any model simulation time. Observed large-scale advective tendencies of temperature, moisture, and horizontal momentum are used as the main large-scale forcings that govern the GCE model in a semiprognostic manner (Soong and Ogura 1980). These are applied uniformly over the model domain with the assumption that the model domain is much smaller than the large-scale disturbance. Large-scale advective tendencies for potential temperature θ and specific humidity q are defined as

$$\left(\frac{\partial T}{\partial t}\right)_{\mathrm{LS}} = -\mathbf{v}_{\mathrm{obs}} \cdot \boldsymbol{\nabla} T_{\mathrm{obs}} - \omega_{\mathrm{obs}} \frac{\partial T_{\mathrm{obs}}}{\partial p} + \frac{\alpha_{\mathrm{obs}}}{C_p'} \omega_{\mathrm{obs}} \qquad (1)$$

and

$$\left(\frac{\partial q}{\partial t}\right)_{\mathrm{LS}} = -\mathbf{v}_{\mathrm{obs}} \cdot \boldsymbol{\nabla} q_{\mathrm{obs}} - \omega_{\mathrm{obs}} \frac{\partial q_{\mathrm{obs}}}{\partial p} \qquad (2)$$

and were derived every 6 h from the version-2.1 TOGA COARE intensive flux array (IFA)-averaged soundings of Ciesielski et al. (2003). Here, $\mathbf{v}$ is the horizontal wind vector, ω is vertical pressure velocity, α is the specific volume, and $C_p' = C_{\mathrm{pd}}(1 - q_{\mathrm{obs}}) + C_{\mathrm{pv}} q_{\mathrm{obs}}$ is the moisture-weighted heat capacity at constant pressure, where C_{pq} and C_{pv} are the heat capacity at constant pressure for dry air and water vapor, respectively. The version-2.1 analysis uses the National Center for Atmospheric Research (NCAR) Atmospheric Technology Division

(ATD) humidity-corrected sonde data (Wang et al. 2002).

Because accurate calculations of the large-scale horizontal momentum forcing terms are difficult to obtain from observations in the Tropics, the terms are instead replaced by a nudging term

$$\left(\frac{\partial \mathbf{v}}{\partial t}\right)_{\mathrm{LS}} = -\frac{\overline{\mathbf{v}} - \mathbf{v}_{\mathrm{obs}}}{\tau}, \qquad (3)$$

where $\overline{\mathbf{v}}$ is the model domain–averaged horizontal velocity, $\mathbf{v}_{\mathrm{obs}}$ is the observed large-scale horizontal vector over the IFA region, and τ is the specified adjustment time scale of approximately 1 h (Grabowski et al. 1996; Xu and Randall 1996). This method constrains the domain-averaged horizontal velocities to follow the observed values and thereby provides a simple means of controlling the cloud system dynamics by the large-scale momentum and shear. Cyclic lateral boundary conditions are incorporated to ensure that there is no additional heat, moisture, or momentum forcing.

For the simulations in this paper, four subperiods with 9-day durations (10–18 December 1992, 27 December 1992–4 January 1993, 9–17 February 1993, and 18–26 February 1993), and one subperiod with an 8-day duration (19–26 December 1992), during the TOGA COARE intensive observation period (IOP) are chosen. The simulations have been done with a data sampling frequency of 5 min.

b. Latent heating

In diagnostic studies (e.g., Yanai et al. 1973; Yanai and Johnson 1993), it is customary to define the *apparent heat source* Q_1 of a large-scale system by averaging horizontally the thermodynamic equation as

$$Q_1 \equiv \overline{\pi}\left[\frac{\partial\overline{\theta}}{\partial t} - \left(\frac{\partial\theta}{\partial t}\right)_{\mathrm{LS}}\right], \qquad (4)$$

where $\pi = (p/P_{00})^{R/C_p}$ is the nondimensional pressure, P_{00} is the reference pressure (1000 hPa), C_p is the specific heat of dry air at constant pressure, and R is the gas constant for dry air. The second term in the parentheses in Eq. (4) is the large-scale advection term given by Eq. (3). The Q_1 can be directly related to the contributions of cloud effects, which can be explicitly estimated by the cloud-resolving model:

$$Q_1 = \overline{\pi}\left(-\frac{1}{\overline{\rho}}\frac{\partial\overline{\rho}\,\overline{w'\theta'}}{\partial z} + \overline{D}_\theta\right) + \overline{\mathrm{LH}} + \overline{Q}_R. \qquad (5)$$

The overbars denote horizontal averages, the primes indicate deviations from the horizontal averages, $\overline{\rho}$ is the air density, Q_R is the cooling/heating rate associated with radiative processes, and D_θ is the subgrid-scale (smaller than the cloud scale) diffusion, which is usually small in comparison with other terms above the boundary layer (Soong and Tao 1980). The first term on the right-hand side of Eq. (5) is the vertical eddy heat flux convergence from upward and downward cloud motions. The term LH is the net latent heating due to the phase change of water:

$$\mathrm{LH} = \frac{L_v}{C_p}(c - e) + \frac{L_f}{C_p}(f - m) + \frac{L_s}{C_p}(d - s), \qquad (6)$$

where L_v, L_f, and L_s are the latent heats of vaporization, fusion, and sublimation, respectively. Variables c, e, f, m, d, and s stand for the rates of condensation, evaporation, freezing of raindrops, melting of snow and graupel, deposition of ice particles, and sublimation of ice particles, respectively. The vertical integration of $Q_1 - \overline{Q}_R$ (hereinafter represented as Q_{1R}) from the surface to the tropopause z_t yields (Yanai et al. 1973)

$$\int_0^{z_t} \rho Q_{1R}(z)\Delta z = \frac{L_v}{C_p}P_0 + \frac{S_0}{C_p}, \qquad (7)$$

where P_0 and S_0 are the surface precipitation rate and surface sensible heat fluxes. The surface sensible heat fluxes are generally smaller than the surface precipitation rate and can be neglected.

The precipitation falling at a given time is not related to latent heating that is occurring at that instant, but rather to the accumulated latent heating that led up to the precipitation over a finite time period. Therefore, LH and Q_{1R} should be basically integrated over the time periods encompassing the life cycles of cloud processes producing the precipitation. However, it is extremely difficult to tabulate, for example, the effect of individual mesoscale systems. Instead, we here depend on the statistics. In the CRM simulation, as well as in the real world, cloud systems develop and decay. Although instantaneous matching between a certain rainfall profile and a heating profile is an ill-posed concept, statistical tabulation still could be done if the life cycle of cloud systems is realistically reproduced in the CRM. For example, a shallow convective rain profile may be at a developing stage of a mesoscale system with a certain probability A, and may be just an isolated convection with a probability of $1 - A$. The latent heating associated with the two cases should be different. However, if the CRM reproduces the statistics of the rain systems well enough, CRM-based tables can statistically represent an average heating profile for a certain rain profile. Besides, we accumulate LH and Q_{1R} over a period of 5 min for each data sampling, because accumulation over long periods is inadequate for moving convective systems. Additional sensitivity tests with periods of 1 and 2 min do not alter the overall results of our study. Hereinafter, heating (LH and Q_{1R}) accumulated over a period of 5 min for each data sampling is represented as instantaneous heating.

The SLH algorithm aims to estimate LH and Q_{1R} for each precipitation profile. Although the PR footprint-scale (4 km) estimates of Q_{1R} are less meaningful because Q_{1R} is a large-scale variable, we still need to derive

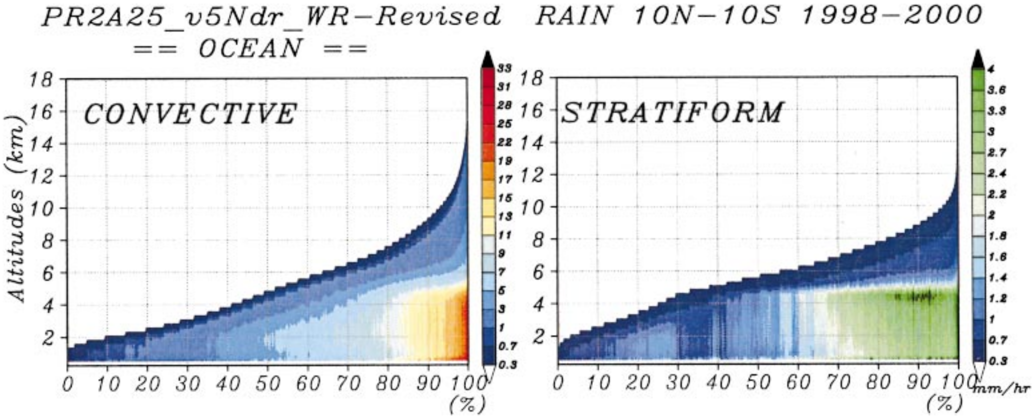

FIG. 2. Cumulative plots of TRMM PR-observed precipitation profiles stratified with PTH from (left) convective and (right) stratiform regions. The abscissa is cumulative frequency and the ordinate is altitude, and the precipitation rate is indicated with color shades. Thresholds of 0.3 mm h^{-1} are used for the precipitation-top detection. The panels are the same as in Fig. 1 of Takayabu (2002), but with a reclassification of shallow, isolated rain (rain type 15 in product 2A23) into convective rain after the suggestion by Schumacher and Houze (2003), utilizing all nadir data over the ocean in the 10°N–10°S belt for the 3 yr of 1998–2000 from PR2A25 version 5.

the value Q_{1R} in order to compare with Q_1 derived from the diagnostic studies for validation. On the other hand, for the footprint-scale estimates, LH is more meaningful than $Q_1 - \overline{Q}_R$. Therefore, we will show the results mainly with LH in this paper.

3. Algorithm development

In this section, we first discuss the classification of rain types, which is essential to the algorithm. Second, we show how lookup tables are constructed. Section 3c describes how these lookup tables are applied to precipitation data in order to retrieve heating profiles.

a. Classification of rain types

Takayabu (2002) separated convective and stratiform precipitation based on the TRMM PR version-5 2A23 convective–stratiform separation algorithm, which classified shallow, isolated precipitation elements into the stratiform category. Recently, Schumacher and Houze (2003) suggested that because the shallow, isolated echoes represent warm-rain processes, they should be classified as convective. After their suggestion we revised spectral plots of Takayabu (2002, her Fig. 1) and present them as Fig. 2, with a reclassification of shallow, isolated rain (rain type 15 in product 2A23) into convective rain. The abscissa is cumulative frequency. Precipitation profiles with a 0.3 mm h^{-1} precipitation-top threshold were accumulated and stratified with PTHs. All nadir precipitation profiles over the ocean in the 10°N–10°S belt for the 3 yr of 1998–2000 from PR2A25 version 5 are used. A shallow stratiform category still exists in Fig. 2. This is because when a bright band exists or the convective reflectivity threshold is not met, shallow and nonisolated rain pixels are classified into stratiform rain (J. Awaka 2003, personal communication).

The TRMM PR rain-type classifications, in which brightband identification is very important, cannot be directly applied to GCE outputs (Awaka et al. 1996). This is because the microphysical schemes utilized in CRMs (e.g., Lin et al. 1983; Rutledge and Hobbs 1984) typically do not contain an explicit description of partially melted precipitation particles that leads to a bright band of enhanced radar reflectivity. Thus, the GCE convective and stratiform separation method (Lang et al. 2003) is used with some modifications to produce the lookup tables from the CRM simulation data in this study.

The GCE method begins with the method of Churchill and Houze (1984) applied to surface rainfall. Model grid points that have a precipitation rate 2 times as large as the value of the background average are identified as convective cores. The points surrounding the core point are also convective, as is any point with a precipitation rate above 20 mm h^{-1}. The background average is taken from a box that has five grid points on a side. Following this, two additional criteria are applied to identify active convection aloft with little or no surface rainfall, such as tilted updrafts and new cells ahead of a convective line (Tao et al. 1993b). Nonsurface precipitation regions are considered to be convective if cloud water exceeds a certain threshold (i.e., the minimum of either 0.5 g kg^{-1} or one-half of the maximum cloud water at that specific simulation time), or if the updraft exceeds a certain threshold (i.e., the minimum value between 3 m s^{-1} and one-half of the maximum updraft at that specific simulation time) below the melting level.

Although the TRMM PR rain-type classification cannot be directly applied to them, we need to maintain the consistency. As shown in Fig. 3, the GCE method has a stratiform category that exists below the 0°C level (grid points with rain index 1 and 4; see Table 1 for the

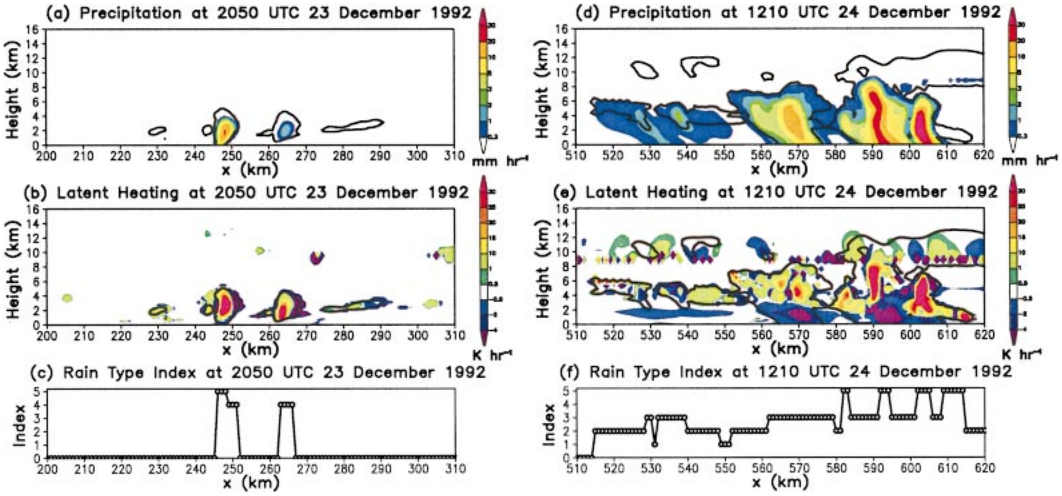

FIG. 3. Snapshots of (a) precipitation rate, (b) latent heating rate superposed on cloud line (boldface line), defined as the region in which the mixing ratio of condensates exceeds 0.1 g kg^{-1}, and (c) rain-type index at 2050 UTC 23 Dec 1992 from the TOGA COARE simulation. (d)–(f) Same as (a)–(c), except at 1210 UTC 24 Dec 1992. Precipitation consists of rain, snow, and graupel. Latent heating is accumulated over a period of 5 min. See Table 1 for the definition of the rain index.

definition of rain index). These shallow rain grid points, in which surface rainfall, cloud water, or updraft do not exceed the above thresholds, are classified into the stratiform category. However, in the same way that rain-type 15 in product 2A23 is reclassified from stratiform to convective, we would like to reclassify the shallow, isolated rain grids (e.g., $x = 264$ km to $x = 267$ km in Figs. 3a–c) as being convective. As for shallow and nonisolated rain grids, we also reclassified them based on their adjacent rain types. The grid points of shallow precipitation (e.g., $x = 249$ km to $x = 251$ km in Figs. 3a–c) adjacent to or surrounded by the convective grid points are classified as being convective. As a result, the grid points with rain index 4 in Figs. 3a–c are reclassified from stratiform into convective. Their heating profiles are characterized by lower-level warming topped by cooling, such as shallow convection in the ‘‘episodic trade wind regimes’’ observed during TOGA COARE (Johnson and Lin 1997). On the other hand, the shallow rain grid points (e.g., $x = 549$ km to $x = 551$ km in Figs. 3d–f) adjacent to or surrounded by deep stratiform precipitation with PTH higher than the melting level (hereinafter the term ‘‘anvil’’ represents deep stratiform regions both with and without surface precipitation) are classified as being stratiform. As a result, the grid points with rain index 1 in Figs. 3d–f remain in a stratiform category. Their heating profiles are characterized by lower-level cooling and upper-level heating.

TABLE 1. The definition of rain index.

Index	GCE method	Modified GCE method
5	Convective	Convective
4	Stratiform	Convective
3	Stratiform	Deep stratiform with surface rain
2	Stratiform	Deep stratiform with no surface rain
1	Stratiform	Shallow stratiform
0	No rain	No rain

All GCE-simulated precipitation profiles with a 0.3 mm h^{-1} precipitation-top threshold are accumulated and stratified with PTH (Fig. 4), as well as the spectral plot of TRMM PR–observed precipitation profiles in Fig. 2. The abscissa is cumulative frequency. Actual numbers of sampled profiles for convective (stratiform) precipitation are 304 205 (2 528 451) or (11:89). Spectral properties of GCE-simulated convective precipitation profiles in Fig. 4 correspond well to those of TRMM PR–observed ones in Fig. 2, having a smooth increase of precipitation intensity with an increase of PTH. Precipitation rates of the GCE-simulated convective precipitation profiles are stronger than those of the PR-observed ones, which could be due to regional differences. The GCE-simulated precipitation profiles are from the TOGA COARE simulations, while the PR-observed ones are from all nadir data over ocean areas in the 10°N–10°S belt.

On the other hand, properties of the GCE-simulated stratiform precipitation profiles show less similarity to those of the PR-observed ones. While the downward decrease of the precipitation rates below the melting layer is indicated in the GCE-simulated stratiform precipitation, as well as the PR-observed ones, the upward rapid decrease of those above the melting layer in the PR-observed precipitation is not indicated in the GCE-simulated stratiform precipitation. This is mainly because the PR can neither retrieve the small ice-phase precipitation nor observe the PTH accurately enough in the upper-level regions of the anvils where small ice-

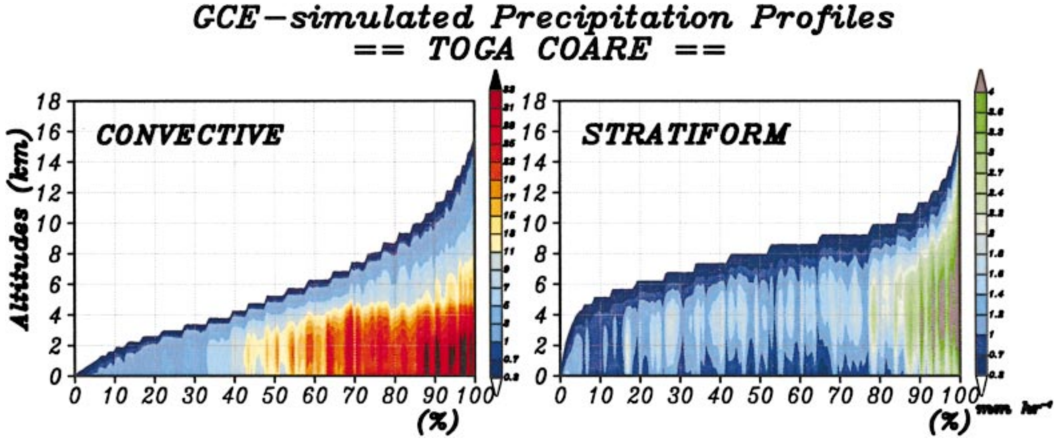

FIG. 4. Same as Fig. 2, but for GCE-simulated precipitation profiles.

phase hydrometors dominate. Thus, insensitivity of the PR to the small ice-phase precipitation should be taken into account by the algorithm.

b. *Construction of lookup tables*

Heating-profile lookup tables have been constructed for the three rain types—convective, shallow stratiform, and deep stratiform both with and without surface rain (Figs. 5 and 6). For the construction of lookup tables, the GCE-simulated precipitation profiles and corresponding heating profiles from the four subperiods with 9-day durations (10–18 December 1992, 27 December 1992–4 January 1993, 9–17 February 1993, and 18–26 February 1993) are used. Another simulation for the one subperiod with an 8-day duration (19–26 December 1992) is not used for the construction of lookup tables, but it is later used for the consistency check of the algorithm.

The PTH is used as an index for the table for convective rain (Figs. 5a and 6a). The GCE-simulated precipitation profiles with a 0.3 mm h^{-1} precipitation-top threshold and corresponding heating profiles are accumulated and averaged for each PTH with model grid

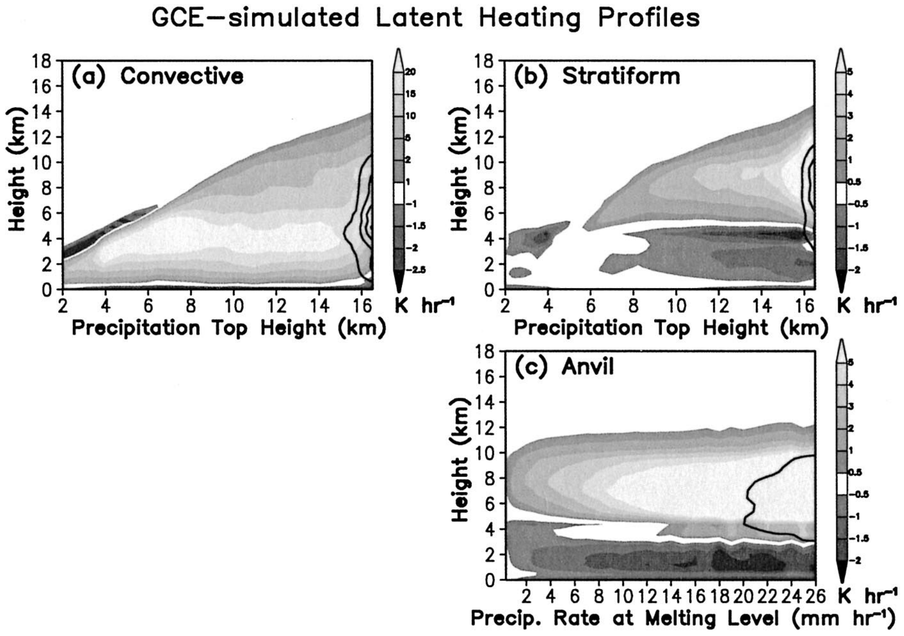

FIG. 5. Ensemble mean, GCE-simulated latent heating profiles, plotted as functions of PTH from (a) convective and (b) stratiform regions, and (c) precipitation rates at the melting level from anvil regions. Contours indicate values of the confidence interval for the mean at the 95% level with Student's *t* test. Contour interval is 2.0 K h^{-1} for convective and 1.0 K h^{-1} for stratiform and anvil profiles. Thresholds of 0.3 mm h^{-1} are used for the precipitation-top detection.

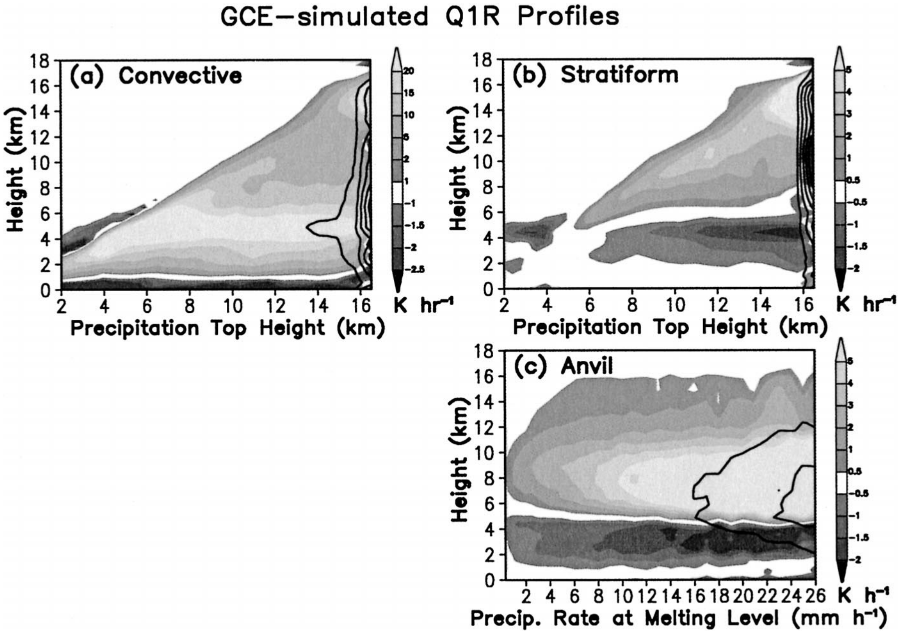

FIG. 6. As in Fig. 5, but for Q_{1R}.

intervals. Properties of convective heating profiles show near-monotonic changes with PTH, so that it is appropriate to use the PTH as an index for tables for convective rain. The levels of Q_{1R} heating maximums are higher than those of the LH heating maximums because of the eddy heat flux convergence [the first term on the right-hand side of Eq. (5)], but the difference between LH and Q_{1R} is not so large. This is because LH is a major contributer to Q_{1R} (Tao et al. 1993b). The LH heating is largely due to condensation and deposition in the convective updrafts, and LH cooling is largely due to rain evaporation found in the lowest levels just above the surface. The level of the LH peak shifts upward until the PTH reaches 6 km and then reaches its plateau around 4 km, just below the melting level (4.4 km). These results indicate that liquid water processes (i.e., condensation) dominate. This is consistent with the results from videosonde observations during TOGA COARE (Takahashi et al. 1995). Notice that the shallow convective heating profiles (PTH < 6 km) are characterized by a cooling aloft, such as the episodic trade wind regimes observed during TOGA COARE (Johnson and Lin 1997). We use these heating profiles (shown in Figs. 5a and 6a) as the convective heating profile lookup table for the SLH algorithm, except for heating profiles with a PTH higher than 16.5 km, whose confidence level for the mean is low because of the small number of profiles.

As for the stratiform precipitation, the GCE-simulated precipitation profiles with a 0.3 mm h^{-1} precipitation-top threshold and corresponding heating profiles are also averaged for each PTH (Figs. 5b and 6b). However, as mentioned earlier, we cannot expect the PR to retrieve the small ice-phase precipitation and observe the PTH accurately enough in the upper-level regions of the anvils where small ice-phase hydrometors dominate. Therefore, only the stratiform heating profiles with a PTH lower than 4.4 km (shown in Figs. 5b and 6b), characterized by lower-level cooling, are used as the shallow stratiform heating profile lookup table for the SLH algorithm.

As shown in Figs. 5b and 6b, the anvil profiles with a PTH higher than the melting level are characterized by upper-level warming and lower-level cooling, which is also found in observations (e.g., Johnson and Young 1983). The upper-level warming in these anvil regions is largely due to condensation and deposition, while the lower-level cooling is largely due to the evaporation of raindrops and melting of ice particles (Tao et al. 1990). As an analogy to Eq. (7), the vertically integrated heating $Q =$ (LH, Q_{1R}), from the melting level z_m to the tropopause z_t, may be related to the precipitation rate at the melting level P_m by

$$\int_{z_m}^{z_t} \rho Q(z) \Delta z = \frac{L_v}{C_p} P_m (1 - f), \tag{8}$$

where f is the fraction of the precipitation rate at the melting level P_m, which is carried over from the convective region. The increases of the upper-level heating amplitude with P_m in Figs. 5c and 6c are consistent with Eq. (8). The PR can measure the precipitation rate at the melting level as can a surface-based radar (e.g., Leary and Houze 1979), although it cannot observe the PTH accurately enough in the upper-level regions of the anvils. Thus, we replace PTH with the precipitation rate

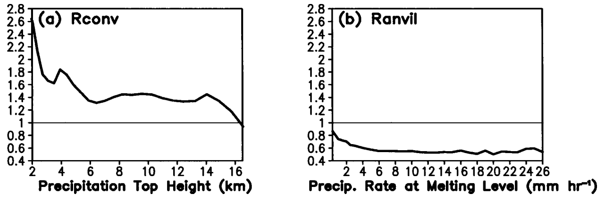

FIG. 7. The ratios R_{conv} and R_{anvil} defined as Eqs. (9) and (10).

at the melting level P_m as the index in the lookup table for anvil regions (Figs. 5c and 6c). It is noted that the Q_{1R} heating is larger than the LH heating above the 12-km level because of the eddy heat flux convergence, which is induced by the radiative cooling at the top of anvil clouds (Sui et al. 1994).

The fraction f to be used in Eq. (8) is not negligible and is examined here. Houze et al. (1980), Gamache and Houze (1983), and Chong and Hauser (1989) showed that the stratiform precipitation falling into the melting layer from the anvil cloud above is a combination of condensate generated in and carried over from the convective region plus condensate that is produced by the anvil region's own upward motion, analyzing the water budgets of a precipitating tropical mesoscale convective system. In order to evaluate this advection effect, we calculated the following values for the convective and anvil tables (Figs. 5a and c):

$$R_{\mathrm{conv}} = \frac{C_p}{L_v}\int_0^{z_t} \frac{\rho \mathrm{LH}(z)\Delta z}{\tilde{P}_s} \quad \text{and} \qquad (9)$$

$$R_{\mathrm{anvil}} = \frac{C_p}{L_v}\int_{z_m}^{z_t} \frac{\rho \mathrm{LH}(z)\Delta z}{\tilde{P}_m} = 1 - f. \qquad (10)$$

Here, P_s is the precipitation rate at the observable lowest level and tildes denote the variables in the lookup table. Although not shown here, the simulated precipitation profiles are also accumulated and averaged as well as the simulated heating profiles. As shown in Fig. 7, R_{conv} is larger than unity and R_{anvil} is smaller than unity, which indicate the contribution to the anvil water budget made by the horizontal transfer of condensate from the convective region. It is noted that R_{conv} decreases with PTH. Convection with low PTH includes shallow convection that is growing into deep convection. Generally, in such growing shallow convection an updraft carries the growing particles upward, because these particles are not yet heavy enough to overcome the updraft (see Fig. 2 of Houze 1981). Thus, total condensates generated in shallow convection are much larger than surface precipitation, which results in large R_{conv}. On the other hand, R_{anvil} decreases with $\tilde{P}_m$. The index of $\tilde{P}_m$ may be interpreted as the distance from the convective region: large $\tilde{P}_m$ indicates a small distance from the convective region, while small $\tilde{P}_m$ indicates a large distance. Close to the convective region, because condensate carried over from the convective region is large, $\tilde{P}_m$ is large and R_{anvil} is small. Condensate carried over from the convective region continues to grow, mainly because of condensation and deposition, and begins to fall relative to the ground. Thus, condensate carried over from the convective region decreases with the distance from the convective region. This accounts for small $\tilde{P}_m$ and large R_{anvil} far from the convective region. The height of maximum heating decreases slightly with $\tilde{P}_m$ in Figs. 5c and 6c, which may be a manifestation of ascending front-to-rear flow and consistent with the above interpretation.

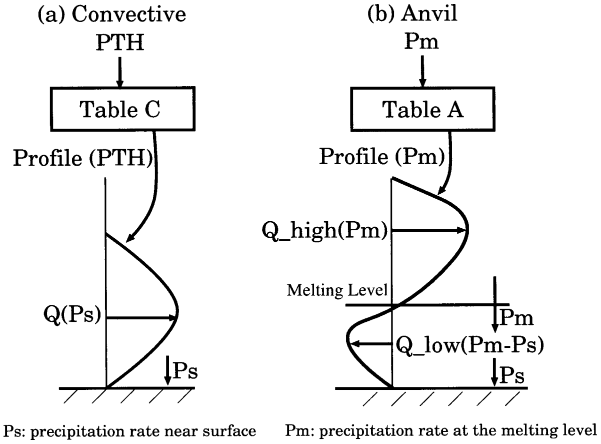

FIG. 8. Diagram showing the procedure for deriving latent heating profiles using the SLH algorithm. See the text for details.

c. Procedure of heating retrieval

In order to retrieve heating profiles, the SLH algorithm utilizes the observed information on precipitation type (convective or stratiform), PTH, P_s, and P_m. The stratiform region is first separated into a shallow stratiform region and an anvil region based on the PTH in comparison with the melting level. The algorithm then derives heating profiles based on the following procedure for each of the three regions (Fig. 8).

For convective regions, as well as shallow stratiform regions, a heating profile corresponding to the PTH is selected in the convective heating-profile (Figs. 5a and 6a) and PTH-based shallow stratiform heating-profile (Figs. 5b and 6b) lookup tables, respectively. Based on Eq. (7), the amplitude is determined by

$$Q(z) = \frac{\tilde{Q}(z)}{\tilde{P}_s} P_S. \qquad (11)$$

For anvil regions with the melting level (PTH > 4.4 km), on the other hand, the heating profile corresponding to P_m is selected in the anvil heating-profile lookup table (Figs. 5c and 6c). The upper-level warming amplitude is then determined by

$$Q_{\mathrm{high}}(z) = \frac{\tilde{Q}_{\mathrm{high}}(z)}{\tilde{P}_m} P_m. \qquad (12)$$

It should be noted that the contribution by the horizontal transfer of condensate from the convective region to the anvil region (i.e., R_{conv}, R_{anvil}) is already included in the lookup tables. This is because $\tilde{Q}(z)$ and $\tilde{Q}_{\text{high}}(z)$ are normalized by $\tilde{P}_s$ and $\tilde{P}_m$ in Eqs. (11) and (12), respectively. Because R_{conv} is larger than unity and R_{anvil} is smaller than unity, as shown in Fig. 7, the vertically integrated amount of $Q(z)$ is estimated to be larger than P_s in the convective regions, while that of $Q_{\text{high}}(z)$ is estimated to be smaller than P_m in the anvil regions.

The evaporative cooling rate below the melting level in the anvil regions is proportional to the reduction of the precipitation profile toward the surface from the melting level (Tao et al. 1990). The downward decrease of the intensity of anvil rain below the melting layer has been statistically indicated in the PR observation (see Fig. 2 of Takayabu 2002), as well as in case studies of traditional radar observations (e.g., Leary and Houze 1979). Thus, the algorithm computes the lower-level cooling amplitude Q_{low} as a function of the difference of the rainfall rate between the surface and the melting level $P_m - P_s$:

$$Q_{\text{low}}(z) = \frac{\tilde{Q}_{\text{low}}(z)}{\tilde{P}_m - \tilde{P}_s}(P_m - P_s). \tag{13}$$

The above procedure allows us to estimate the heating profiles in the anvil regions both with and without surface precipitation.

4. Consistency check

a. Comparison with the GCE model

For a consistency check of the SLH algorithm, we reconstructed heating profiles averaged over the TOGA COARE IFA region for the 19–26 December 1992 period using the simulated parameters (i.e., PTH, convective/stratiform characteristics, P_s, P_m) as inputs. The simulated data during 19–26 December 1992 are independent from other simulated data that are used for the construction of lookup tables. This period is characterized by the transitions among cloud regimes and has also been used by the Global Energy and Water Cycle Experiment (GEWEX) Cloud System Study (GCSS) working group 4 (WG4) model intercomparison project for CRMs and single-column models (SCMs, Moncrieff et al. 1997). Tao et al. (2000) showed that there was excellent agreement between heating profiles derived from the sounding and simulated by the GCE model. Then, the algorithm-reconstructed heating profiles from GCE-simulated precipitation profiles are compared with GCE-simulated true heating profiles, which are computed directly from the model thermodynamic equation (Fig. 9).

Figures 9a and 9d show the time series of the simulated heating and reconstructed heating, respectively. Here we show only the results for LH. The results of Q_{1R} are similar to those of LH. The pattern in temporal variations of the SLH algorithm-reconstructed heating profile agrees well with that of the GCE-simulated heating profile. In particular, the SLH algorithm-reconstructed heating profiles captured the evolution of a quasi-2-day oscillation (Takayabu et al. 1996) during the period of 1800 UTC 23 December–1800 UTC 25 December 1992. During the period 1800 UTC 23 December–1200 UTC 24 December, the transition from the shallow convective stage to the deep convective stage can be seen in the GCE-simulated as well as in the reconstructed LH profiles. During 0600–1500 UTC 25 December, both simulated and reconstructed LH profiles show upper-level heating and lower-level cooling. It is noted that the reconstructed results show more smoothed features. This is because the lookup tables represented the averaged profiles for each index, either PTH or $\tilde{P}_m$.

Figures 9b and 9e show the time series of the simulated heating and reconstructed heating in the convective regions, respectively. The pattern in temporal variations of the reconstructed heating profile agrees very well with that of the simulated heating profile. The differences between the shallow convective stage and the deep convective stage are realistically reconstructed. This is a result of the utilization of observed information, not only on precipitation type and intensity, but also on the precipitation depth (i.e., PTH).

Figures 9c and 9f show the time series of the simulated heating and reconstructed heating in the stratiform regions (shallow stratiform plus anvil), respectively. Although the reconstructed time series are smoother than the simulated ones, the pattern in temporal variations of the reconstructed heating profile agrees well with that of the simulated heating profile. For example, there is no surface rain in the stratiform region around 1200 UTC 25 December, as shown later (Fig. 14), because hydrometers generated at the middle and upper levels evaporate completely before reaching the surface. Still, the SLH algorithm reconstructs the heating profiles characterized by upper-level heating and lower-level cooling around 1200 UTC, consistent with the GCE simulations. This comes from utilizing the precipitation rate at the melting level (P_m) for anvil rain. The SLH algorithm gives smoother features of the reconstructed heating time series for the stratiform regions than those for the convective regions. This is because in the lookup table the heating profile does not vary much with P_m for anvil rain (Figs. 5c and 6c).

Eight-day-averaged profiles of the simulated LH and the reconstructed LH are shown in Figs. 10a and 10b. These profiles are simply the time averages of the profiles shown in Fig. 9. The 8-day-averaged profiles of the reconstructed LH agree very well with the simulated ones in total, convective, and stratiform regions, although the reconstructed convective heating above the melting level is a little bit stronger than the simulated one. Also, the 8-day-averaged profiles of the reconstructed Q_{1R} (Fig. 10d) agree very well with the simulated ones in the total, convective, and stratiform regions (Fig. 10c). Both simulated and reconstructed LH profiles have a distinct cooling near 4.4 km, which is due to the

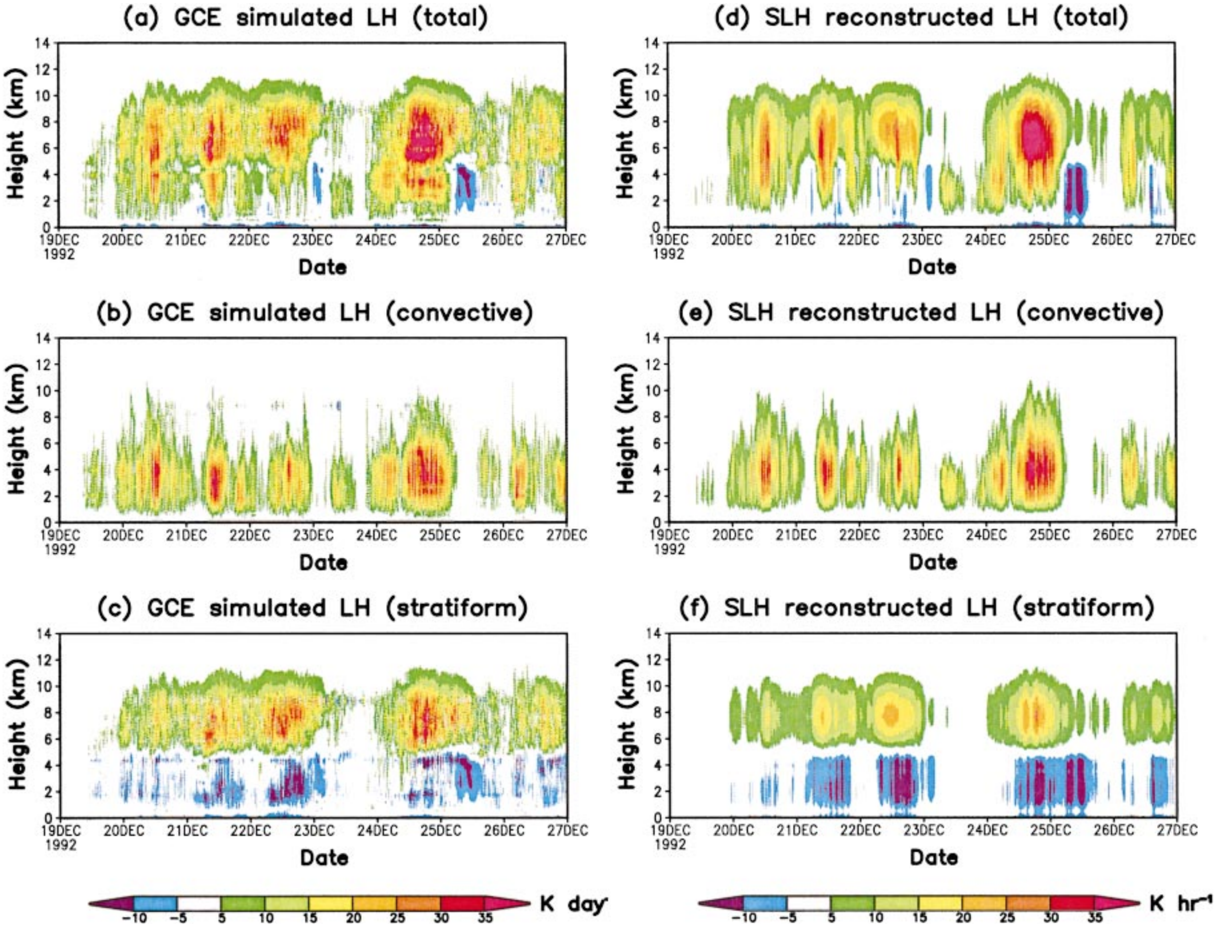

FIG. 9. Time series of LH profiles averaged over the TOGA COARE IFA region for the 19–26 Dec 1992 period. (a) Simulated from the GCE model. The GCE model simulated LH over (b) the convective and (c) stratiform regions. (d)–(f) Same as (a)–(c), except reconstructed using the SLH algorithm with the lookup tables shown in Fig. 5.

melting processes. On the other hand, neither the simulated nor reconstructed Q_{1R} profile has such a distinct cooling near 4.4 km. This is because the eddy heat flux convergence compensates for the distinct cooling due to the melting (Sui et al. 1994; Shie et al. 2003).

b. Estimation errors

Based on the assumption that heating profiles correspond statistically to precipitation profiles or precipitation parameters (i.e., PTH, P_m), we construct lookup tables. However, instantaneous heating structures are very fluctuating. Here, we reconstructed the heating profiles grid by grid for the four 9-day subperiods that were used for the lookup tables, using the simulated parameters as inputs. Then, the differences between reconstructed heating profiles and simulated ones are examined statistically to see the errors of instantaneous and grid-by-grid estimates with this table method. It serves as a guide in the application of the algorithm and interpretation of the results. The discussion of errors due to regional or seasonal change is beyond the scope of this study and will be discussed in the forthcoming Part II.

Figure 11 shows histograms of grid numbers per χ (reconstructed LH − simulated LH) for the lower ($z = 3.5$ km) and upper ($z = 7.6$ km) levels, in which convective heating and stratiform heating have their maximum, respectively. Grid points where nonzero heating is simulated by the GCE model or reconstructed by the SLH algorithm are used for the plots. Figure 11 indicates that for grid-by-grid estimation in the convective regions, there are errors that are quite large at 3.5 km, while those at 7.6 km considered small. It is noted that at 7.6 km in convective regions, the number of grid points with $\chi > 0$ K h^{-1} (overestimation) is larger than those grid points with $\chi < 0$ K h^{-1} (underestimation). This is consistent with the results of the consistency check shown in Fig. 10 where the reconstructed convective heating above the melting level is a little stronger than the simulated one. On the other hand, at 7.6 km in the stratiform region, the number of grid points with $\chi < -10$ K h^{-1} is larger than those with $\chi > 10$ K h^{-1}, while the number of grid points with 0 K h^{-1}

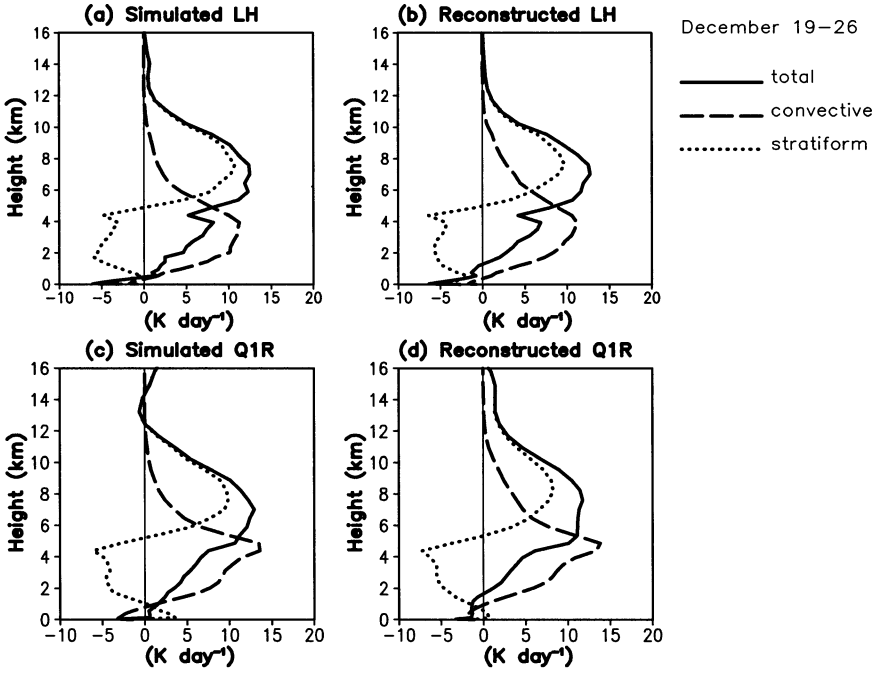

FIG. 10. Eight-day averaged profiles of LH rate and Q_{1R} in total (solid), convective (dashed), and stratiform (dotted) regions for the 19–26 Dec 1992 period. (a) Simulated LH from the GCE model. (b) Reconstructed LH using the SLH algorithm with the lookup tables shown in Fig. 5. (c) Same as (a), but for Q_{1R}. (d) Same as (b), but for Q_{1R} using the SLH algorithm with the lookup tables shown in Fig. 6.

$< \chi < 5$ K h^{-1} is larger than those of grid points with -5 K h^{-1} $< \chi < 0$ K h^{-1}. This is because the SLH algorithm cannot capture the large heating associated with old convective cells remaining in the upper levels of the trailing stratiform regions. These results suggest that the SLH algorithm estimates should be averaged for quantitative use.

A preliminary evaluation of the horizontally averaged estimates is also performed using a GCE-simulated synthetic observation (Fig. 12). Horizontal averaging reduces the root-mean-square (rms) error, and for averaging over an ~50 km width the rms error is reduced to about 1 K^2 h^{-2}. From this result, an averaging over an ~50 km width is recommended when using the SLH algorithm estimates quantitatively. Large rms errors can be found at about 9 km. Again, this may be because the SLH algorithm cannot capture large heating associated with old convective cells remaining in the upper levels of the trailing stratiform regions.

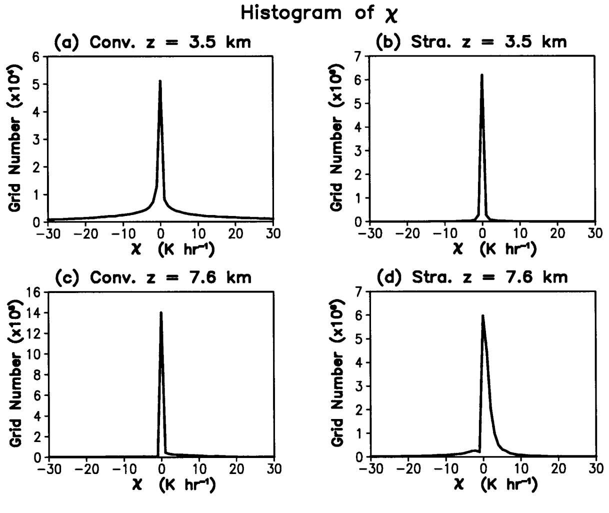

FIG. 11. Histograms of grid numbers per χ (SLH algorithm-reconstructed LH $-$ GCE-simulated LH). (a) Convective and (b) stratiform regions at $z = 3.5$ km. (c), (d) Same as (a), (b) but for $z = 7.6$ km.

c. Comparison with the CSH algorithm

Tao et al. (2001) represented the first attempt at using TRMM rainfall information to estimate the latent heating structure over the global Tropics for February 1998. Three different latent heating algorithms—the HH algorithm, the CSH algorithm, and the GPROF heating algorithm—were used and their results were intercompared. The CSH algorithm-estimated heating profiles only showed one maximum heating level and were in better agreement in diagnostic studies than the HH algorithm- or GPROF algorithm-estimated heating profiles. Only for one of the three algorithms, the CSH algorithm, can PR product be used as input, as well as the TMI products. Here, we compare the SLH algorithm performance with the CSH algorithm performance, using the simulated parameters as inputs. Because the re-

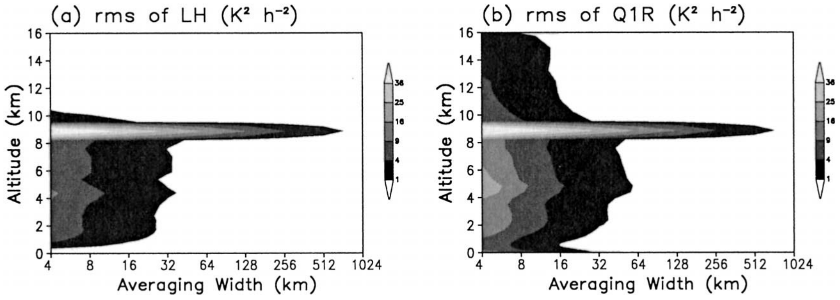

FIG. 12. The rms error in the horizontally averaged heating profiles between the SLH algorithm-reconstructed and the GCE-simulated (a) LH and (b) Q_{1R}.

sults of both methods are derived from the same model, the comparison of SLH and CSH is not a rigorous test, but rather a consistency check. Its purpose is to see their advantages and disadvantages purely originating from the different retrieval procedures between SLH and CSH.

The CSH algorithm has been developed based on the assumption that the shape of the overall MCS heating profile is determined by the relative amounts of convective and mesoscale heating, which are proportional to the relative amounts of convective and stratiform precipitation:

$$Q(z) = P_{\rm conv}Q(z)_{\rm conv} + P_{\rm stra}Q(z)_{\rm stra}. \qquad (14)$$

Here, $P_{\rm conv}$ and $P_{\rm stra}$ are observed surface precipitation rates in the convective and stratiform regions, and $Q(z)_{\rm conv}$ and $Q(z)_{\rm stra}$ are model-generated convective and stratiform heating profiles, normalized by the convective and stratiform rainfall, respectively. An appropriate selection of latent heating profiles from the lookup table is very important for the CSH algorithm (Tao et al. 2000).

Figures 13a–c show the time series of the LH profiles simulated by the GCE model and reconstructed by the SLH algorithm, and the CSH algorithm during 19–26 December 1992, respectively. Eight-day-averaged convective and stratiform LH profiles during 19–26 December 1992 (Fig. 10a), normalized by the convective and stratiform rainfall, respectively, are used for the CSH algorithm to reconstruct LH profiles from simulated $P_{\rm conv}$ and $P_{\rm stra}$. Clearly this is the most adequate set of heating profiles. Figure 13, however, indicates that the SLH algorithm reconstructs the time series of the heating profile better than the CSH algorithm, especially for the period of 1800 UTC 23 December–1800 UTC 25 December 1992 when the evolution of a quasi-2-day oscillation can be seen. During the period 1800 UTC 23 December–1200 UTC 24 December, the transition from the shallow convective stage to the deep convective stage can not be seen in the CSH algorithm reconstructed LH profiles. In addition, during 0600–1500 UTC 25 December, the CSH algorithm-reconstructed LH profiles is negligible, while the GCE-simulated and the SLH algorithm-reconstructed LH profiles show upper-level heating and lower-level cooling.

Figure 14 shows the time series of precipitation rates during the period of 1800 UTC 23 December–1800 UTC 25 December when the evolution of a quasi-2-day oscillation can be seen. The subperiods in Figs. 14a–d indicate shallow convective, developing, mature, and decaying stages of the quasi-2-day oscillation, respec-

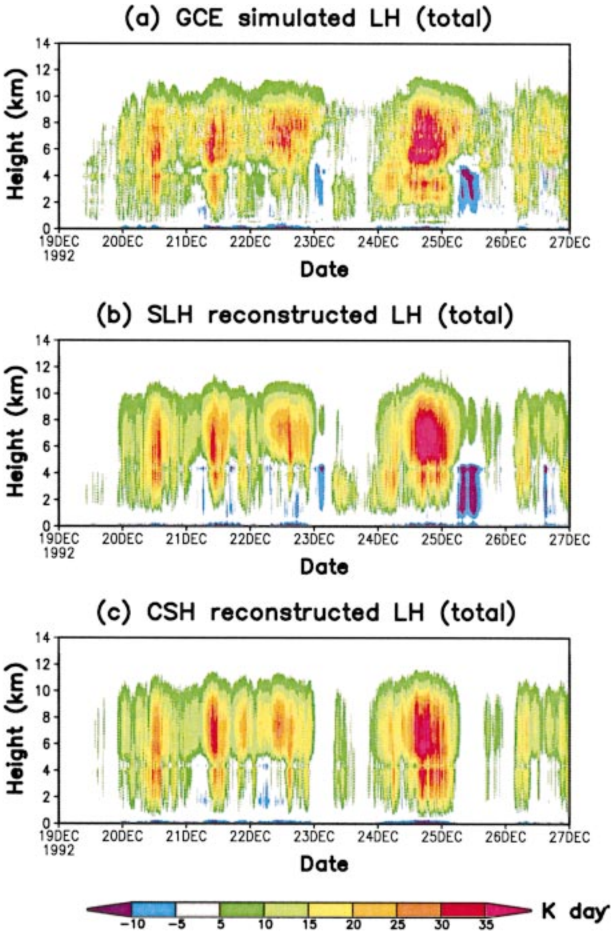

FIG. 13. Same as Fig. 9, but for (a) simulated from the GCE model, (b) reconstructed using the SLH algorithm, and (c) reconstructed latent heating profiles using the CSH algorithm.

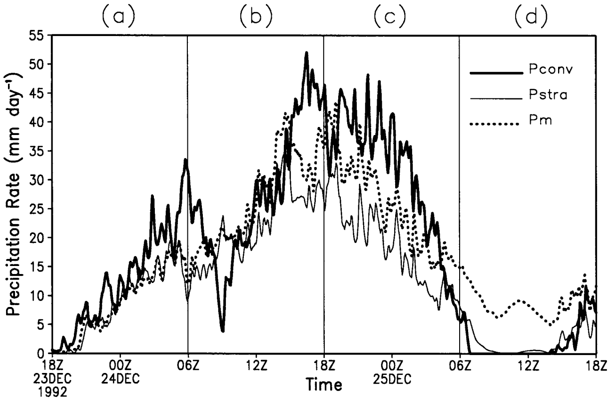

FIG. 14. Time series of precipitation rate for the 1800 UTC 23 Dec–1800 UTC 25 Dec 1992 period, simulated by the GCE model. The boldface and thin solid lines represent the convective and stratiform components of the surface precipitation rate, respectively. The precipitation rate at the melting level in the stratiform region is plotted with the dotted line. The (a) shallow convective, (b) developing, (c) mature, and (d) decaying stages of the quasi-2-day oscillation are identified.

tively. Figures 15a–d show LH profiles for the subperiods of Figs. 14a–d, respectively.

During the shallow convective stage the cloud ensemble with low PTH dominated (see Figs. 3a–c). The SLH-reconstructed LH profile with maximum below the melting level is in good agreement with that simulated by the GCE model. In contrast, the CSH algorithm reconstructed LH profile was at a maximum above the melting level (Fig. 15a). The underestimation of low-level heating made by the CSH algorithm is caused by two reasons. First, the CSH algorithm fixes the convective heating profile in the 8-day-averaged profile (Fig. 10a), and, thus, cannot retrieve a shallow convective profile. Second, the ratio of total convective heating to surface precipitation (i.e., $\tilde{R}_{\mathrm{conv}}$) for shallow convection is much larger than that for deep convection, as is shown in Fig. 7. In the CSH algorithm, because the convective heating profile is normalized by the averaged convective rainfall, the ratio of total convective heating to surface precipitation is also fixed in the 8-day-averaged profile, which is smaller than that of shallow convection, and the heating amplitude only varies because of the convective component of the surface precipitation rate (P_{conv}). These account for the underestimation of low-level heating.

During the developing stage, both the SLH and CSH algorithms reconstructed the LH profile in good agreement with that simulated by the GCE model (Fig. 15b). It is noted that both the SLH and CSH algorithms reconstructed somewhat stronger upper-level heating and weaker lower-level heating than those simulated by the GCE model because of the underestimation of convective heating and overestimation of anvil heating. This may be because the contribution to the anvil water budget made by the horizontal transfer of condensate from the convective region simulated by the GCE model is more than that assumed by both algorithms in their tables, which results in an underestimation of convective heating and an overestimation of anvil heating.

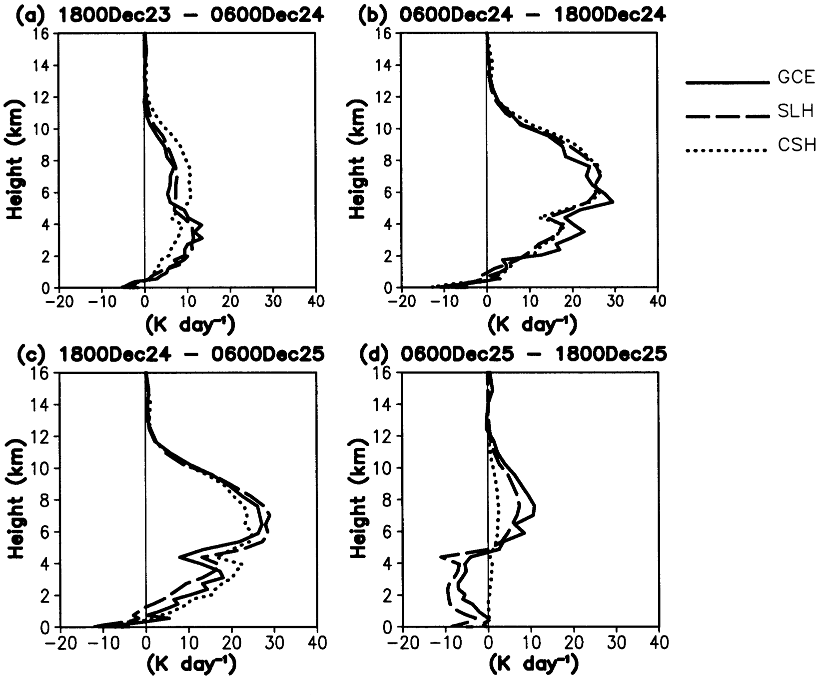

FIG. 15. Latent heating rate profiles for each 12-h period during 1800 UTC 23 Dec–1800 UTC 25 Dec 1992, simulated by the GCE model (solid line), reconstructed by the SLH algorithm (long-dashed line), and reconstructed by the CSH algorithm (dotted line).

During the mature stage, the GCE model simulated LH profile (Fig. 15c) is similar to that at the developing stage (Fig. 15b), but the lower-level amplitude at the mature stage should be smaller than that at the developing stage. This is due to lower-level cooling resulting from increasing anvil rainfall. The SLH algorithm-reconstructed LH profile with a maximum at 7 km is in good agreement with the GCE model simulation. In contrast, the CSH algorithm-reconstructed LH profile has a tendency to underestimate in the upper levels and to overestimate in the lower levels. It is because the relative contribution of P_{stra} to total surface precipitation at the mature stage is smaller than at the developing stage, as shown in Fig. 14.

The decaying stage includes a period when P_{stra} is zero. The CSH algorithm reconstructed the LH profile with a very small amplitude. This is because the CSH algorithm estimates no heating profiles from the no-surface rain [see Eq. (14)]. On the other hand, the SLH algorithm-reconstructed LH profile characterizes upper-level heating and lower-level cooling in good agreement with the GCE model simulation (Fig. 15d). This is because the SLH algorithm can compute heating profiles from the precipitation rate at the melting level in the stratiform region (P_m). It is noted that the melting-level cooling in this decaying stage is stronger in the reconstructed profile than in the simulated profile.

These results show that the utilization of PTH and P_m provides two distinct advantages for the SLH algorithm. First, the differences in heating profiles between the shallow convective stage and the deep convective stage can be realistically retrieved. Second, heating profiles in the decaying stage with no surface rain can also be retrieved.

The CSH algorithm takes into account the fact that when cloud latent heating is separated into convective and stratiform regions, the profiles for each region take on a characteristic shape, even for systems from different geographic locations (Johnson 1984; and a review by Houze 1997). Therefore, the CSH algorithm is best used for temporal scales over the lifetime of a system. For example, the 2-day-averaged profile of LH reconstructed by the CSH algorithm for the period covering the entire life time of the quasi-2-day oscillation (1800 UTC 23 December–1800 UTC 25 December) is in good agreement with that simulated by the GCE model, as well as that reconstructed by the SLH algorithm (Fig. 16). It is, however, inferred from the disagreement between the CSH algorithm-reconstructed and the GCE-simulated LH profiles during the shallow convective stage shown in Fig. 15a, that even for monthly averaged heating profiles the CSH algorithm may not retrieve the heating features unless it used the "representative" heating profiles normalized by surface rain rate. Tao et al. (2001) showed that the CSH algorithm-retrieved heating profile over the Atlantic Ocean for 1 month has an upper-level (about 8 km) heating maximum and is not in agreement with a distinct, single midlevel (about 4–5 km) heating maximum seen in the mean heating profile determined from a diagnostic budget study during the Global Atmospheric Research Program (GARP) Atlantic Tropical Experiment (GATE)[2] (Nitta 1978; Thompson et al. 1979). The reasons for the disagreement between the CSH algorithm-reconstructed and the GCE-simulated LH profiles during the shallow convective stage shown in Fig. 15a explain the disagreement between the CSH algorithm-retrieved and the diagnostically determined profiles over the Atlantic Ocean.

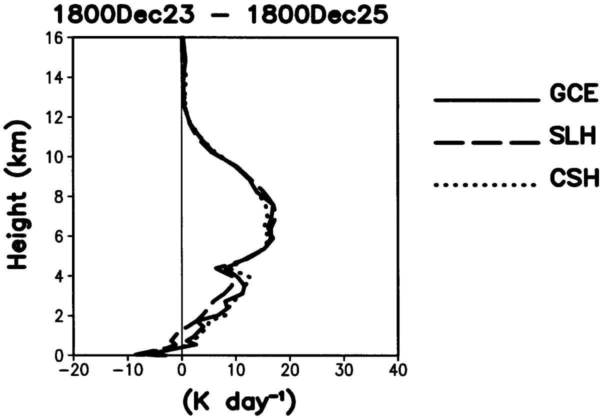

FIG. 16. As in Fig. 15, but for the 2-day average during the period of 1800 UTC 23 Dec–1800 UTC 25 Dec 1992.

Tao et al. (2000, their Fig. 16) showed that the CSH algorithm-retrieved heating profiles for the 19–26 December 1992 period, computed using the convective and stratiform heating profile associated with the February convective period in TOGA COARE, results in more cooling at the lower levels and larger heating at the upper levels. They suggested that this is because the cooling below and heating aloft are greater in the stratiform region for February than for December. For a preliminary evaluation of the SLH algorithm's sensitivity to the selection of the lookup tables, we reconstructed the heating profiles for 19–26 December 1992 using the lookup table produced only from the February simulations (i.e., 9–17 February 1993 and 18–26 February 1993). Figure 17 shows the GCE-simulated and the SLH algorithm-reconstructed heating profiles. The 8-day-averaged SLH algorithm-reconstructed profiles are in good agreement with the GCE-simulated ones in total, convective, and stratiform regions, although the reconstructed convective heating profile is somewhat higher than the simulated one. These results indicate that the SLH algorithm is less sensitive to the selection of the lookup table than is the CSH algorithm. This is primarily because the lookup table of the SLH algorithm prepares multiple profiles of latent heat release for various PTHs, while the CSH algorithm depends on two averaged vertical profiles of latent heat release for convective and

---

[2] GATE was conducted in the tropical Atlantic Ocean in 1974.

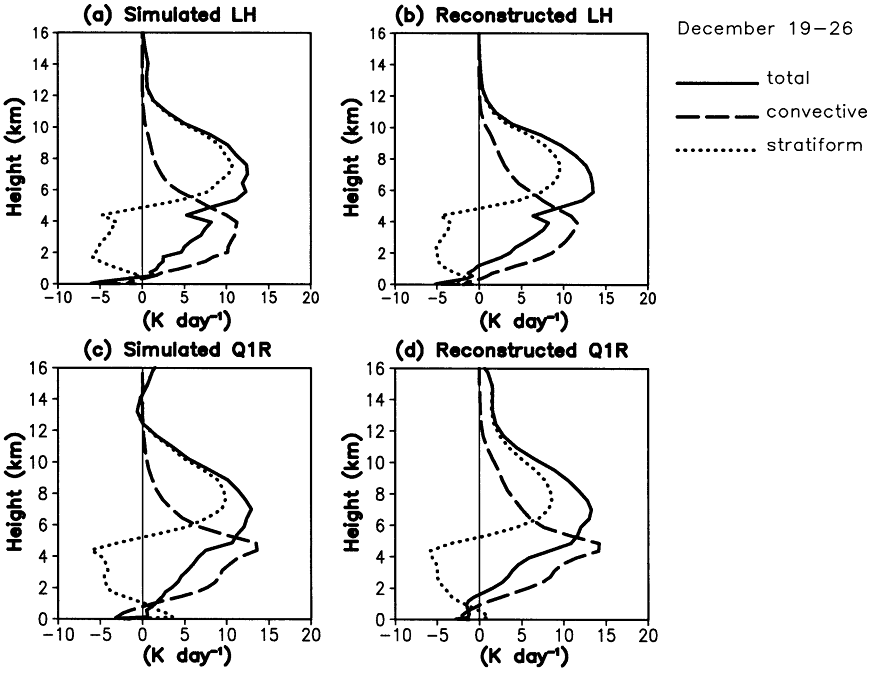

FIG. 17. Same as Fig. 10, but for (b) LH and (d) Q_{1R}, which are reconstructed by the SLH algorithm with the lookup tables from the 9–17 Feb 1993 and 18–26 Feb 1993 simulations.

stratiform regions. Second, it is because the SLH algorithm uses not only P_s, but also P_m. However, it is necessary to examine the universality of the lookup table by simulations of other field experiments [e.g., GATE, the South China Sea Monsoon Experiment (SCSMEX),[3] and the Kwajalein Experiment (KWAJEX)[4]] for global application of the SLH algorithm to the TRMM PR data.

5. Summary and future work

The spectral representation of rain profiles observed by the precipitation radar of the Tropical Rainfall Measuring Mission satellite provides details about convective and stratiform rain characteristics over the equatorial area (Takayabu 2002). Based on these spectral statistics of TRMM PR data, we introduce a new retrieval algorithm (the spectral latent heating algorithm) for the PR data.

Numerical simulations of cloud systems in the TOGA COARE IFA were conducted using observed large-scale advective temperature and moisture forcings. To construct the lookup tables, GCE-simulated precipitation profiles and corresponding heating profiles from the four subperiods with 9-day durations (10–18 December 1992, 27 December 1992–4 January 1993, 9–17 February 1993, and 18–26 February 1993) are used. Those from the one subperiod with an 8-day duration (19–26 December 1992) are set aside to serve as ‘‘observed’’ fields for the consistency check of the algorithm.

The heating profiles are sorted according to the precipitation-top height of convective and stratiform regions. Considering the sensitivity of the PR, we used a threshold of 0.3 mm h^{-1} to determine the PTH. Properties of the convective heating profiles show near-monotonic change with PTH, so that it is appropriate to use PTH as an index for tables for convective rain. Stratiform heating profiles consist of two groups. One group includes shallow stratiform heating profiles (PTH $<$ 4.4 km), characterized by lower-level cooling. The other group consists of anvil heating profiles (PTH $>$ 4.4 km), characterized by upper-level warming and lower-level cooling. We cannot obtain the PTH accurately enough for the anvil regions because of the insensitivity of PR to the small ice-phase hydrometors. Therefore, we selected the precipitation rate at the melting level instead of PTH as a parameter for the lookup table for the anvil regions.

For a consistency check of the SLH algorithm, we reconstructed latent heating profiles for 19–26 December 1992 with the lookup tables. Patterns in temporal variations of simulated heating profiles and reconstructed ones agree very well. Differences between the shallow convective stage and the deep convective stage are reconstructed more realistically than with other algorithms currently used. This is because we prepare spectral vertical profiles of latent heat release for various PTHs. The heating profile in the decaying stage with no surface precipitation can also be retrieved. This

---

[3] SCSMEX was conducted in the northern South China Sea in 1998.

[4] KWAJEX was conducted on the Kwajalein atoll in 1999.

comes from utilizing the precipitation intensity at the melting level for anvil rain.

One might infer that the SLH algorithm (i.e., lookup tables) is tied to a specific CRM—the GCE model used in this study. Krueger and Lazarus (1999) showed the similarities in the bulk characteristics between the observations and the results from the several CRMs that participated in the GCSS WG4 case-2 study. This is because the same observed forcing data (time varying), large-scale advective tendencies of potential temperature, water vapor mixing ratio, and horizontal momentum were used as the main forcing as well as in this study. However, even if the same forcing data are used, we might find the differences among lookup tables from the CRMs. For example, the differences in ice microphysics among the CRMs might affect the use of the 0.3 mm h^{-1} threshold. Comparisons of lookup tables from the CRMs using the same forcing data might be interesting not only for the SLH algorithm, but also for the CRMs intercomparison.

For global application of the SLH algorithm to TRMM PR data, it is necessary to examine the universality or regionality of the lookup table. As suggested by Houze (1989), the vertical profile of heating for convection of a given depth may vary from location to location. For example, convective cells with enhanced liquid water processes (i.e., condensation) have latent heating concentrated below the freezing level, whereas convective cells with significant ice processes (i.e., riming and/or depositional growth) should provide stronger latent heating above the freezing level. We are now extending our study to simulations of other field experiments (e.g., GATE, SCSMEX, and KWAJEX) in order to examine the universality of the lookup table and will report our results in the forthcoming Part II of this study. We will also perform simulations with Atmospheric Radiation Measurement Program (ARM)[5] data in order to produce lookup tables for precipitation over land.

For a true test, the SLH algorithm will be applied to PR data and the results will be compared with heating profiles derived diagnostically from sounding data of TRMM field experiments (e.g., SCSMEX; Johnson and Ciesielski 2002). Comparisons of the SLH algorithm estimates from TOGA COARE shipborne radar data (Short et al. 1997), with heating profiles derived diagnostically from sounding data during TOGA COARE (Ciesielski et al. 2003), may also be a good test but are left to future studies. It is also planned to compare the SLH algorithm retrieved latent heating profiles with those derived from other methods (Tao et al. 1993a; Olson et al. 1999; Yang and Smith 1999a,b) using TRMM data.

Acknowledgments. The first author expresses special thanks to Chung-Lin Shie for his kind guidance on using the GCE model. He also appreciates discussions with Bill Olson, Song Yang, and Steve Lang during his short-term visit to NASA GSFC, partly supported by a research fellowship from the Japan Society for the Promotion of Science for Young Scientists. This study is supported by the JAXA/EORC Tropical Rainfall Measuring Mission (TRMM) project. Yukari N. Takayabu would like to express her heartfelt gratitude to the late Prof. Tsuyoshi Nitta for motivating her to develop the latent heating algorithm utilizing TRMM PR data. Authors W.-K. Tao and D. E. Johnson are mainly supported by the NASA headquarters Atmospheric Dynamics and Thermodynamics Program and the NASA TRMM. They thank Dr. R. Kakar at NASA headquarters for his support. The authors thank three anonymous reviewers for their constructive comments that improved the clarity of the presentation in this paper. We also thank Paul Ciesielski (CSU) for providing us with the large-scale forcing datasets for the model simulations. The Grid Analysis and Display System (GrADS) package was utilized for the figures. Acknowledgments are also made to JAXA/EORC for computer time used in this research.

REFERENCES

Austin, P. M., and R. A. Houze Jr., 1973: A technique for computing vertical transports by precipitating cumuli. *J. Atmos. Sci.,* **30,** 1100–1111.

Awaka, J., H. Kumagai, T. Iguchi, and K. Okamoto, 1996: Development of an algorithm for classifying rain types (in Japanese). *J. Commun. Res. Lab.,* **42,** 325–337.

——, T. Iguchi, and K. Okamoto, 1998: Early results on rain type classification by the Tropical Rainfall Measuring Mission (TRMM) precipitation radar. *Proc. Eighth URSI Commission F Open Symp.,* Aveiro, Portugal, URSI, 143–146.

Cheng, C. P., and R. A. Houze Jr., 1980: Sensitivity of diagnosed convective fluxes to model assumptions. *J. Atmos. Sci.,* **37,** 774–783.

Chong, M., and D. Hauser, 1989: A tropical squall line observed during the COPT81 experiment in West Africa. Part II: Water budget. *Mon. Wea. Rev.,* **117,** 728–744.

Churchill, D. D., and R. A. Houze Jr., 1984: Development and structure of winter monsoon cloud cluster on 10 December 1978. *J. Atmos. Sci.,* **41,** 933–960.

Ciesielski, P. E., R. H. Johnson, P. T. Haertel, and J. Wang, 2003: Corrected TOGA COARE sounding humidity data: Impact on diagnosed properties of convection and climate over the warm pool. *J. Climate,* **16,** 2370–2384.

Emanuel, K. E., J. D. Neelin, and C. S. Bretherton, 1994: On large-scale circulations in convecting atmospheres. *Quart. J. Roy. Meteor. Soc.,* **120,** 1111–1143.

Gamache, J. F., and R. A. Houze Jr., 1983: Water budget of a mesoscale convective system in the Tropics. *J. Atmos. Sci.,* **40,** 1835–1850.

Gill, A. E., 1980: Some simple solutions for heat-induced tropical circulation. *Quart. J. Roy. Meteor. Soc.,* **106,** 447–462.

Grabowski, W. W., X. Wu, and M. W. Moncrieff, 1996: Cloud-resolving modeling of tropical cloud systems during Phase III of GATE. Part I: Two-dimensional experiments. *J. Atmos. Sci.,* **53,** 3684–3709.

Hartmann, D., H. H. Hendon, and R. A. Houze Jr., 1984: Some implications of the mesoscale circulations in tropical cloud clusters for large-scale dynamics and climate. *J. Atmos. Sci.,* **41,** 113–121.

---

[5] ARM data collected in the southern U.S. Great Plains are utilized.

Houze, R. A., Jr., 1973: A climatological study of vertical transports by cumulus-scale convection. *J. Atmos. Sci.,* **30,** 1112–1123.

——, 1981: Structures of atmospheric precipitation systems: A global survey. *Radio Sci.,* **16,** 671–689.

——, 1982: Cloud clusters and large-scale vertical motions in the Tropics. *J. Meteor. Soc. Japan,* **60,** 396–410.

——, 1989: Observed structure of mesoscale convective systems and implications for large-scale heating. *Quart. J. Roy. Meteor. Soc.,* **115,** 425–461.

——, 1997: Stratiform precipitation in regions of convection: A meteorological paradox. *Bull. Amer. Meteor. Soc.,* **78,** 2179–2196.

——, and C. A. Leary, 1976: Comparison of convective mass and heat transports in tropical easterly waves computed by two methods. *J. Atmos. Sci.,* **33,** 424–429.

——, C.-P. Cheng, C. A. Leary, and J. F. Gamache, 1980: Diagnosis of cloud mass and heat fluxes from radar and synoptic data. *J. Atmos. Sci.,* **37,** 754–773.

Iguchi, T., T. Kozu, R. Meneghini, J. Awaka, and K. Okamoto, 2000: Rain-profiling algorithm for the TRMM precipitation radar. *J. Appl. Meteor.,* **39,** 2038–2052.

Johnson, R. H., 1984: Partitioning tropical heat and moisture budgets into cumulus and mesoscale components: Implications for cumulus parameterization. *Mon. Wea. Rev.,* **112,** 1590–1601.

——, and G. S. Young, 1983: Heat and moisture budgets of tropical mesoscale anvil clouds. *J. Atmos. Sci.,* **40,** 2138–2146.

——, and X. Lin, 1997: Episodic trade wind regimes over the western Pacific warm pool. *J. Atmos. Sci.,* **54,** 2020–2034.

——, and P. E. Ciesielski, 2002: Characteristics of the 1998 summer monsoon onset over the northern South China Sea. *J. Meteor. Soc. Japan,* **80,** 561–578.

Klemp, J., and R. Wilhelmson, 1978: The simulation of three-dimensional convective storm dynamics. *J. Atmos. Sci.,* **35,** 1070–1096.

Kozu, T., and Coauthors, 2001: Development of precipitation radar onboard the Tropical Rainfall Measuring Mission (TRMM) satellite. *IEEE Trans. Geosci. Remote Sens.,* **39,** 102–116.

Krueger, S. K., and S. M. Lazarus, 1999: Intercomparison of multi-day simulations of convection during TOGA COARE with several cloud-resolving and single-column models. Preprints, *23d Conf. on Hurricanes and Tropical Meteorology,* Dallas, TX, Amer. Meteor. Soc., 643–647.

Kummerow, C., and Coauthors, 2000: The status of the Tropical Rainfall Measuring Mission (TRMM) after two years in orbit. *J. Appl. Meteor.,* **39,** 1965–1982.

Lang, S., W.-K. Tao, J. Simpson, and B. Ferrier, 2003: Modeling of convective–stratiform precipitation processes: Sensitivity to partitioning methods. *J. Appl. Meteor.,* **42,** 505–527.

Leary, C. A., and R. A. Houze Jr., 1979: Melting and evaporation of hydrometeors in precipitation from the anvil clouds of deep tropical convection. *J. Atmos. Sci.,* **36,** 669–679.

——, and ——, 1980: The contribution of mesoscale motions to the mass and heat fluxes of an intense tropical convective system. *J. Atmos. Sci.,* **37,** 784–796.

Lin, Y.-L., R. D. Farley, and H. D. Orville, 1983: Bulk parameterization of the snow field in a cloud model. *J. Climate Appl. Meteor.,* **22,** 1065–1092.

Madden, R. A., and P. Julian, 1971: Detection of a 40–50 day oscillation in the zonal wind in the tropical Pacific. *J. Atmos. Sci.,* **28,** 702–708.

——, and ——, 1972: Description of global scale circulation cells in the Tropics with a 40–50 day period. *J. Atmos. Sci.,* **29,** 1109–1123.

——, and ——, 1994: Observations of the 40–50-day tropical oscillation—A review. *Mon. Wea. Rev.,* **122,** 814–837.

Mapes, B. E., 1993: Gregarious tropical convection. *J. Atmos. Sci.,* **50,** 2026–2037.

——, 1997: Equilibrium vs. activation controls on large-scale variations of tropical deep convection. *The Physics and Parameterization of Moist Convection,* R. K. Smith, Ed., NATO ASI Series, Springer, 321–358.

Matsuno, T., 1966: Quasi-geostrophic motions in the equatorial area. *J. Meteor. Soc. Japan,* **44,** 25–43.

Moncrieff, M. W., S. K. Krueger, D. Gregory, J.-L. Redelsperger, and W.-K. Tao, 1997: GEWEX Cloud System Study (GCSS) Working Group 4: Precipitating convective cloud systems. *Bull. Amer. Meteor. Soc.,* **78,** 831–845.

Nitta, T., 1970: A study of generation and convection of eddy available potential energy in Tropics. *J. Meteor. Soc. Japan,* **48,** 524–528.

——, 1972: Energy budget of wave disturbances over the Marshall Island during the years of 1956 and 1958. *J. Meteor. Soc. Japan,* **50,** 71–84.

——, 1978: A diagnostic study of interaction of cumulus updrafts and downdrafts with large-scale motions in GATE. *J. Meteor. Soc. Japan,* **56,** 232–242.

Okamoto, K., 2003: A short history of the TRMM precipitation radar. *Cloud Systems, Hurricanes, and the Tropical Rainfall Measuring Mission (TRMM): A Tribute to Dr. Joanne Simpson, Meteor. Monogr.,* No. 51, Amer. Meteor. Soc., 187–195.

Olson, W. S., C. D. Kummerow, Y. Hong, and W.-K. Tao, 1999: Atmospheric latent heating distributions in the Tropics derived from satellite passive microwave radiometer measurements. *J. Appl. Meteor.,* **38,** 633–664.

Rutledge, S. A., and P. V. Hobbs, 1984: The mesoscale and microscale structure and organization of clouds and precipitation in midlatitude cyclones. XII: A diagnostic modeling study of precipitation development in narrow cold-frontal rainbands. *J. Atmos. Sci.,* **41,** 2949–2972.

Schumacher, C., and R. A. Houze Jr., 2003: The TRMM precipitation radar's view of shallow, isolated rain. *J. Appl. Meteor.,* **42,** 1519–1524.

Shie, C.-L., W.-K. Tao, J. Simpson, and C.-H. Sui, 2003: Quasi-equilibrium states in the Tropics simulated by a cloud-resolving model. Part I: Specific features and budget analysis. *J. Climate,* **16,** 817–833.

Shige, S., and T. Satomura, 2000: The gravity wave response in the troposphere around deep convection. *J. Meteor. Soc. Japan,* **78,** 789–801.

Short, D. A., P. A. Kucera, B. S. Ferrier, J. C. Gerlach, S. A. Rutledge, and O. W. Thiele, 1997: Shipboard radar rainfall patterns within the TOGA COARE IFA. *Bull. Amer. Meteor. Soc.,* **78,** 2817–2836.

Simpson, J., 1992: Global circulation and tropical cloud activity. *The Global Role of Tropical Rainfall,* J. S. Theon et al., Eds., A. Deepak, 77–92.

Soong, S.-T., and Y. Ogura, 1980: Response of tradewind cumuli to large-scale processes. *J. Atmos. Sci.,* **37,** 2035–2050.

——, and W.-K. Tao, 1980: Response of deep tropical clouds to mesoscale processes. *J. Atmos. Sci.,* **37,** 2016–2034.

Stevens, B., D. A. Randall, X. Lin, and M. T. Montgomery, 1997: Comments on ''On large-scale circulations in convecting atmospheres'' by Emanuel, Neelin and Bretherton. *Quart. J. Roy. Meteor. Soc.,* **123,** 1771–1778.

Sui, C. H., K. M. Lau, W.-K. Tao, and J. Simpson, 1994: The tropical water and energy cycles in a cumulus ensemble model. Part I: Equilibrium climate. *J. Atmos. Sci.,* **51,** 711–728.

Takahashi, T., K. Suzuki, M. Orita, M. Tokuno, and R. de la Mar, 1995: Videosonde observations of precipitation processes in equatorial cloud clusters. *J. Meteor. Soc. Japan,* **73,** 509–534.

Takayabu, Y. N., 2002: Spectral representation of rain profiles and diurnal variations observed with TRMM PR over the equatorial area. *Geophys. Res. Lett.,* **29,** 1584, doi:10.1029/2001GL014113.

——, K.-M. Lau, and C.-H. Sui, 1996: Observation of a quasi-2-day wave during TOGA COARE. *Mon. Wea. Rev.,* **124,** 1892–1913.

——, T. Iguchi, M. Kachi, A. Shibata, and H. Kanzawa, 1999: Abrupt termination of the 1997–98 El Niño in response to a Madden–Julian oscillation. *Nature,* **402,** 279–282.

Tao, W.-K., 2003: Goddard Cumulus Ensemble (GCE) model: Application for understanding precipitation processes. *Cloud Systems, Hurricanes, and The Tropical Rainfall Measurement Mis-*

sion (TRMM): A Tribute to Dr. Joanne Simpson, Meteor. Monogr., No. 51, Amer. Meteor. Soc., 107–137.

——, and J. Simpson, 1993: Goddard Cumulus Ensemble model. Part I: Model description. *Terr. Atmos. Oceanic Sci.,* **4,** 35–72.

——, ——, S. Lang, M. McCumber, R. Adler, and R. Penc, 1990: An algorithm to estimate the heating budget from vertical hydrometer profiles. *J. Appl. Meteor.,* **29,** 1232–1244.

——, S. Lang, J. Simpson, and R. Adler, 1993a: Retrieval algorithms for estimating the vertical profiles of latent heat release: Their applications for TRMM. *J. Meteor. Soc. Japan,* **71,** 685–700.

——, J. Simpson, C.-H. Sui, B. Ferrier, S. Lang, J. Scala, M.-D. Chou, and K. Pickering, 1993b: Heating, moisture, and water budgets of tropical and midlatitude squall lines: Comparisons and sensitivity to long radiation. *J. Atmos. Sci.,* **50,** 673–690.

——, S. Lang, J. Simpson, C.-H. Sui, B. Ferrier, and M.-D. Chou, 1996: Mechanisms of cloud-radiation interaction in the Tropics and midlatitudes. *J. Atmos. Sci.,* **53,** 2624–2651.

——, ——, ——, W. Olson, D. Johnson, B. Ferrier, C. Kummerow, and R. Adler, 2000: Vertical profiles of latent heat release and their retrieval for TOGA COARE convective systems using a cloud resolving vodel, SSM/I, and ship-borne radar data. *J. Meteor. Soc. Japan,* **78,** 333–355.

——, and Coauthors, 2001: Retrieved vertical profiles of latent heat release using TRMM rainfall products for February 1998. *J. Appl. Meteor.,* **40,** 957–982.

——, and Coauthors, 2003: Microphysics, radiation and surface processes in the Goddard Cumulus Ensemble (GCE) model. *Meteor. Atmos. Phys.,* **82,** 97–137.

Thompson, R. M., Jr., S. W. Payne, E. E. Recker, and R. J. Reed, 1979: Structure and properties of synoptic-scale wave disturbances in the intertropical convergence zone of the eastern Atlantic. *J. Atmos. Sci.,* **36,** 53–72.

Wang, J., H. L. Cole, D. J. Carlson, E. R. Miller, K. Beierle, A. Paukkunen, and T. K. Laine, 2002: Corrections of humidity measurement errors from Vaisala RS80 radiosonde—Application to TOGA COARE data. *J. Atmos. Oceanic Technol.,* **19,** 981–1002.

Xu, K.-M., and D. A. Randall, 1996: Explicit simulation of cumulus ensembles with the GATE Phase III data: Comparison with observations. *J. Atmos. Sci.,* **53,** 3710–3736.

Yanai, M., and R. H. Johnson, 1993: Impacts of cumulus convection on thermodynamic fields. *The Representation of Cumulus Convection in Numerical Models, Meteor. Monogr.,* No. 46, Amer. Meteor. Soc., 39–62.

——, S. Esbensen, and J.-H. Chu, 1973: Determination of bulk properties of tropical cloud clusters from large-scale heat and moisture budgets. *J. Atmos. Sci.,* **30,** 611–627.

——, B. Chen, and W.-W. Tung, 2000: The Madden–Julian oscillation observed during the TOGA COARE IOP: Global view. *J. Atmos. Sci.,* **57,** 2374–2396.

Yang, S., and E. A. Smith, 1999a: Moisture budget analysis of TOGA COARE area using SSM/I-retrieved latent heating and large-scale Q_2 estimates. *J. Atmos. Oceanic Technol.,* **16,** 633–655.

——, and ——, 1999b: Four-dimensional structure of monthly latent heating derived from SSM/I satellite measurements. *J. Climate,* **12,** 1016–1037.

Yoshizaki, M., 1991: Selective amplification of the eastward-propagating mode in a positive-only wave-CISK model on an equatorial beta plane. *J. Meteor. Soc. Japan,* **69,** 353–373.